The Effects of Process Parameters on Melt-pool Oscillatory Behaviour in Gas Tungsten Arc Welding

Ebrahimi, Amin; Kleijn, C.R.; Hermans, M.J.M.; Richardson, I.M.

DOI
10.1088/1361-6463/abf808

Publication date
2021

Document Version
Final published version

Published in
Journal of Physics D: Applied Physics

Citation (APA)
Ebrahimi, A., Kleijn, C. R., Hermans, M. J. M., & Richardson, I. M. (2021). The Effects of Process Parameters on Melt-pool Oscillatory Behaviour in Gas Tungsten Arc Welding. *Journal of Physics D: Applied Physics*, *54*(27), Article 275303. https://doi.org/10.1088/1361-6463/abf808

OPEN ACCESS
IOP Publishing
Journal of Physics D: Applied Physics
J. Phys. D: Appl. Phys. **54** (2021) 275303 (18pp)
https://doi.org/10.1088/1361-6463/abf808

The effects of process parameters on melt-pool oscillatory behaviour in gas tungsten arc welding

Amin Ebrahimi[1,*], **Chris R Kleijn**[2], **Marcel J M Hermans**[1] **and Ian M Richardson**[1]

[1] Department of Materials Science and Engineering, Faculty of Mechanical, Maritime and
Materials Engineering, Delft University of Technology, Mekelweg 2, 2628 CD Delft, The Netherlands
[2] Department of Chemical Engineering, Faculty of Applied Sciences, Delft University of Technology,
van der Maasweg 9, 2629 HZ Delft, The Netherlands

E-mail: A.Ebrahimi@tudelft.nl

Received 14 February 2021, revised 26 March 2021
Accepted for publication 14 April 2021
Published 29 April 2021

Abstract

Internal flow behaviour and melt-pool surface oscillations during arc welding are complex and not yet fully understood. In the present work, high-fidelity numerical simulations are employed to describe the effects of welding position, sulphur concentration (60–300 ppm) and travel speed (1.25–5 $\mathrm{mm\,s^{-1}}$) on molten metal flow dynamics in fully-penetrated melt-pools. A wavelet transform is implemented to obtain time-resolved frequency spectra of the oscillation signals, which overcomes the shortcomings of the Fourier transform in rendering time resolution of the frequency spectra. Comparing the results of the present numerical calculations with available analytical and experimental datasets, the robustness of the proposed approach in predicting melt-pool oscillations is demonstrated. The results reveal that changes in the surface morphology of the pool resulting from a change in welding position alter the spatial distribution of arc forces and power-density applied to the molten material, and in turn affect flow patterns in the pool. Under similar welding conditions, changing the sulphur concentration affects the Marangoni flow pattern, and increasing the travel speed decreases the size of the pool and increases the offset between top and bottom melt-pool surfaces, affecting the flow structures (vortex formation) on the surface. Variations in the internal flow pattern affect the evolution of melt-pool shape and its surface oscillations.

Supplementary material for this article is available online

Keywords: fusion welding, positional welding, weld-pool behaviour, surface oscillations, numerical simulation

(Some figures may appear in colour only in the online journal)

1. Introduction

Fusion joining of metallic materials is an essential requirement in many industries. The integrity of products depends critically on the joining technique employed and the quality of the joints produced [1, 2], which in turn is influenced by the dynamic stability of the melt-pool [3]. A better understanding of the complex transport phenomena inside melt-pools offers considerable opportunities for improved monitoring and control of

---

[*] Author to whom any correspondence should be addressed.

joining processes. To date, control and optimisation of welding processes relies largely on trial-and-error experiments that often pose challenges due to the non-linearity of melt-pool responses to changes in operating conditions, material properties and process parameters [4–6]. Moreover, welding process development requires tolerance to parameter variations, within which the resultant weld integrity must be fit for the intended purpose, irrespective of the particular parameter combinations within the defined procedural range.

The present work focuses on positional gas tungsten arc (GTA) welding, which involves several significant operating parameters, the number increasing when complex time-dependent phenomena are considered [7]. The simulation-based approach utilised in the present work offers the potential to reduce procedure development costs and will enhance our understanding of melt-pool behaviour during positional GTA welding.

The majority of published studies on GTA melt-pool oscillatory behaviour are experimentally based, consider only the flat (1G or PA) welding orientation (i.e. position C1 shown in figure 1) and focus on processing the signals received from the melt pool to sense penetration [8]. Experimental techniques employed are often based on laser vision [9], arc voltage [10] or arc-light intensity [11] measurements. A critical limitation is related to the inadequate signal-to-noise ratio for low-amplitude surface oscillations [12], which makes the application of a triggering action essential [13]. Moreover, these techniques ignore convection in the melt pool, which is difficult to measure due to opacity, the fast dynamic response of the molten metal flow and high temperatures [1]. In addition to the experimental measurements, analytical models have been developed to predict dominant oscillation frequencies. These models are based on similarities between oscillations of the melt-pool surface and the vibrations of a thin stretched membrane [10, 11, 14–16]. Unfortunately, the absolute accuracy of these analytical models is critically dependent on the melt-pool shape, temperature-dependent material properties and processing conditions [12], which in turn are affected by unsteady transport phenomena in the pool [17]; factors that are not known *a priori*. Moreover, changes in oscillation mode and amplitude are not predictable using these models. Conversely, high-fidelity numerical simulations have demonstrated a remarkable potential to describe the complex internal flow behaviour in melt pools and associated surface deformations [18, 19].

Although many numerical models are available (e.g. [20–27]), numerical studies on melt-pool surface oscillations are scarce and the melt-pool oscillatory behaviour is not yet fully understood, particularly for positional welding conditions. Previous studies often focused on the influence of surface deformations on the melt-pool shape [28–32] or the morphology of the melt-pool surface, to study ripple formation [33], welding defects such as undercut [34] or humping [35–37]. Chen *et al* [38] revealed that the flow patterns in pools with one free surface, representative of partially penetrated welds, differ from those in pools with two free surfaces, representative of fully penetrated welds. In their model, they neglected solidification and melting, assumed that the flow inside the pool is axisymmetric and that the surface tension of the molten material is a linear function of temperature. Using a similar model, including electromagnetic forces and solid-liquid phase transformations, Ko *et al* [39, 40] showed that pool oscillations during stationary GTA welding depend on the direction of the Marangoni flow. For many real-world welding applications, non-pure materials are involved for which the surface tension changes non-linearly with temperature [41]. This coupled with movements of the melt-pool boundaries due to solid-liquid phase transformations form complex unsteady flow patterns that are inherently three-dimensional [42–44], affecting the melt-pool surface oscillations.

In our previous study on stationary GTA welding [18], we demonstrated that changes in welding current and material properties can alter the time-frequency response of melt-pool oscillations under both partial and full penetration conditions. The welding position can also influence the shape of the deformations of the melt-pool surface and its shape during GTA welding [45, 46]. Moreover, morphology of the melt-pool surface can affect the spatial and temporal distribution of arc-pressure and power-density and thus the melt-pool dynamic behaviour [18, 39]. Further investigations are essential to broaden our understanding of complex internal flow behaviour in melt pools and melt-pool surface oscillations in positional GTA welding. In the present study, the results of numerical simulations employed to reveal complex unsteady transport phenomena in the melt-pool and associated surface oscillations during positional GTA welding are reported. The present study focuses particularly on fully-penetrated pools, where the melt-pool oscillations are critical for process stability; however, the present model is equally applicable to partial penetration conditions. The coupling between melt-pool surface deformations, arc force and power-density distributions, which represent physical realism and can affect the predicted thermal and flow fields, are taken into account. The continuous wavelet transform is applied to the time-resolved displacement signals acquired from the simulations to enhance our understanding of the evolution of surface oscillations and its correlation with process parameters and material properties. A novel insight into the evolution of melt-pool surface oscillations and the complex flow inside molten metal melt pools is provided, which offers a computational approach to fusion welding process development and optimisation.

2. Problem description

Molten metal flow behaviour and associated surface oscillations during positional gas tungsten arc welding of a stainless steel (AISI 316) plate are studied numerically. As shown schematically in figure 1, the plate has a thickness of $H_\mathrm{m} =$ 2 mm and is heated locally by an electric arc plasma to create a melt pool in the plate that is initially at $T_0 = 300$ K. A perpendicular torch is adopted for all positions in line with automated pipeline welding. The current is set to 85 A and the initial arc length (electrode tip to workpiece distance) before igniting the arc is 2.5 mm. Obviously, the melt-pool surface deforms during the process, leading to changes in the length, voltage and power of the arc as well as power-density distribution and the magnitude and distribution of forces induced by the arc plasma [18, 47, 48]. In the present model, the melt-pool is decoupled from the arc plasma to reduce the computation time and complexity of simulations. Accordingly, the related source terms for momentum and thermal energy are adjusted dynamically in the present model to take these changes into account, as explained in section 3. Argon gas is employed to shield the melt-pool. The temperature-dependent thermophysical properties of AISI 316 and argon are presented in table 1. The temperature-dependent surface tension of the molten material is modelled using an empirical correlation introduced in (21) Sahoo *et al* [41], which accounts for the influence of surface-active elements (i.e. sulphur).

A moving reference frame is employed in the present numerical simulations to simulate unsteady convection in the melt pool. Hence, instead of moving the heat source, the material enters the computational domain, translates at a fixed speed (i.e. The welding travel speed) opposite to the welding direction shown in figure 1, and leaves the computational domain. Applying the moving reference frame technique facilitates a decrease in the size of the computational domain and thus the runtime. The computational domain is designed in the form of a rectangular cuboid encompassing the workpiece and two layers of gas below and above the sample to monitor the oscillations of the melt-pool surfaces. The width and the length of the computational domain is $W = 40$ mm and $L = 70$ mm respectively, which is substantially larger than the dimensions of the melt-pool. The boundary conditions applied to the computational domain in the simulations are shown in figure 1(b). The outer boundaries of the workpiece are adiabatic and are treated as no-slip moving walls. The gas layers have a thickness of $H_a = 2$ mm and a fixed atmospheric pressure ($p = p_{\text{atm}} = 101.325$ kPa) is applied to their outer boundaries. The electrode axis is located in the middle of the plate (i.e. $x = W/2$) and 15 mm away from the leading-edge of the plate (i.e. $y = 15$ mm). Eight different welding positions (workpiece orientations with respect to gravity) are studied, as shown in figure 1(c).

3. Methods

3.1. Model formulation

Our previous multiphase model for stationary GTA welding [18] is extended here to predict the complex three-dimensional molten metal flow and melt-pool surface oscillations during positional moving GTA welding. In this model, the molten metal and argon were assumed to be incompressible and were treated as Newtonian fluids. Accordingly, the unsteady governing equations were cast in conservative form as follow:

$$\nabla \cdot \mathbf{u} = 0, \tag{1}$$

Table 1. Thermophysical properties of AISI 316 and argon used in the computational model. T is in Kelvin.

Property	Stainless steel (AISI 316) [49]	Gas (argon)	Unit
Density ρ	7100	1.623	$\text{kg}\,\text{m}^{-3}$
Specific heat capacity c_p	$430.18+0.1792\,T$ (solid phase) 830 (liquid phase)	520.64	$\text{J}\,\text{kg}^{-1}\,\text{K}^{-1}$
Thermal conductivity k	$11.791+0.0131\,T$ (solid phase) $6.49+0.0129\,T$ (liquid phase)	520.64	$\text{W}\,\text{m}^{-1}\,\text{K}^{-1}$
Viscosity μ	6.42×10^{-3}	2.1×10^{-5}	$\text{kg}\,\text{m}^{-1}\,\text{s}^{-1}$
Thermal expansion coefficient β	2×10^{06}	—	K^{-1}
Latent heat of fusion $\mathcal{L}$	2.7×10^{5}	—	$\text{J}\,\text{Kg}^{-1}$
Liquidus temperature T_l	1723	—	K
Solidus temperature T_s	1658	—	K

$$\rho\frac{D\mathbf{u}}{Dt} = \mu\nabla^2\mathbf{u} - \nabla p + \mathbf{F}_\text{d} + \mathbf{F}_\text{s} + \mathbf{F}_\text{b}, \tag{2}$$

$$\rho\frac{Dh}{Dt} = \frac{k}{c_\text{p}}\nabla^2 h - \rho\frac{D(\psi\mathcal{L})}{Dt} + S_\text{q} + S_\text{l}, \tag{3}$$

where ρ is the density, $\mathbf{u}$ the relative velocity vector, t the time, μ the dynamic viscosity, p the pressure, h the sensible heat, k the thermal conductivity, c_p the specific heat capacity at constant pressure, and $(\psi\mathcal{L})$ the latent heat. The total enthalpy of the material $\mathscr{H}$ is the sum of the latent heat $(\psi\mathcal{L})$ and the sensible heat h and is defined as follows [50]:

$$\mathscr{H} = \left(h_\text{r} + \int_{T_\text{r}}^{T} c_\text{p}\,\text{d}T\right) + \psi\mathcal{L}, \tag{4}$$

where T is the temperature, ψ the local liquid volume-fraction, and $\mathcal{L}$ the latent heat of fusion. The subscript 'r' indicates the reference condition. Assuming the liquid volume-fraction ψ to be a linear function of temperature [50], its value can be calculated as follows:

$$\psi = \frac{T - T_\text{s}}{T_\text{l} - T_\text{s}}; \quad T_\text{s} \leqslant T \leqslant T_\text{l}, \tag{5}$$

where T_l and T_s are the liquidus and solidus temperatures, respectively.

To capture the position of the gas-metal interface, the volume-of-fluid (VOF) method [51] was employed, where the scalar function ϕ indicates the local volume-fraction of a phase in a given computational cell. The value of ϕ varies from 0 in the gas phase to 1 in the metal phase, and cells with $0 < \phi < 1$ represent the gas-metal interface. The linear advection

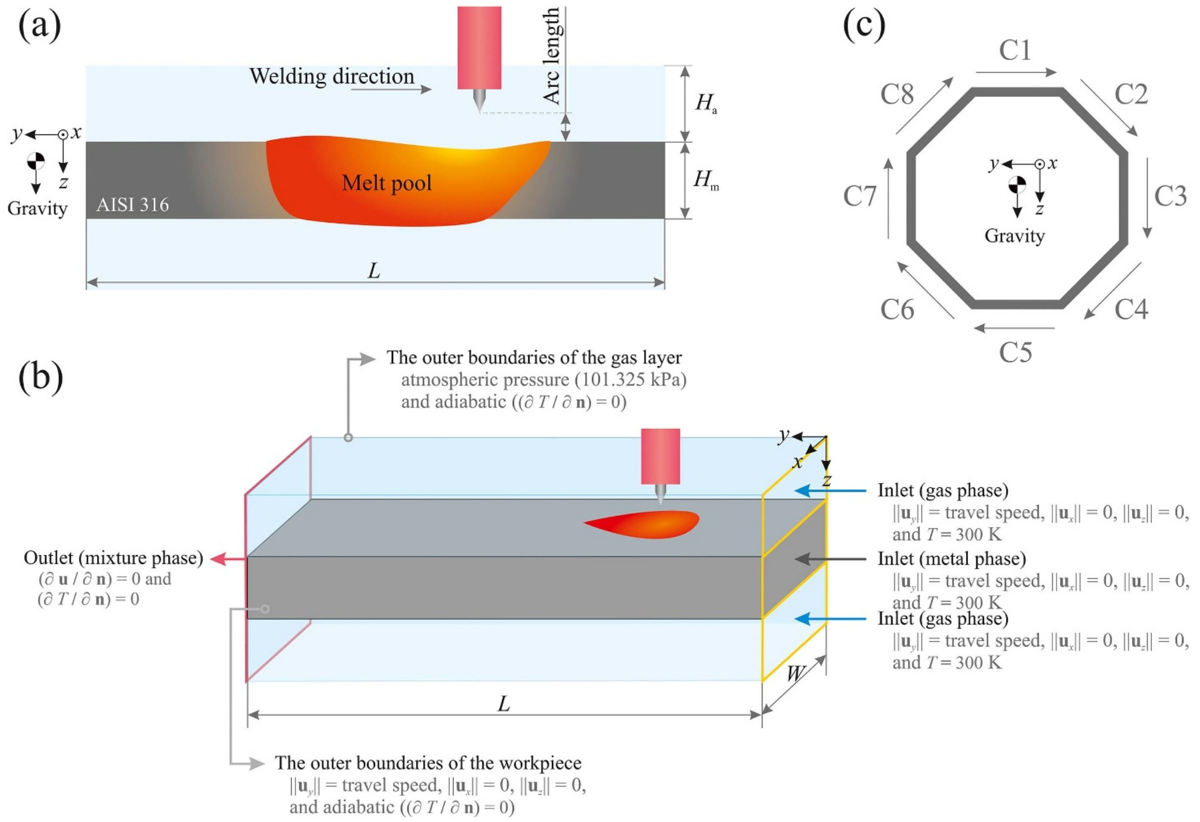

Figure 1. Schematic of moving gas tungsten arc welding (GTAW). (a) A cross section of the plate showing a fully-penetrated melt pool, (b) three-dimensional view of the problem under consideration and (c) different welding positions studied in the present work.

equation describes the advection of the scalar function ϕ as follows:

$$\frac{D\phi}{Dt} + \phi \nabla \cdot \mathbf{u} = 0. \tag{6}$$

Accordingly, the effective thermophysical properties of the material in each computational cell were determined as follows:

$$\xi = \phi \xi_{\mathrm{m}} + (1 - \phi)\, \xi_{\mathrm{g}}, \tag{7}$$

where ξ corresponds to thermal conductivity k, specific heat capacity c_{p}, viscosity μ and density ρ, and subscripts 'g' and 'm' indicate gas or metal respectively.

Solid-liquid phase transformation occurs in the temperature range between T_{s} and T_{l} in the so-called 'mushy zone'. To model the damping of liquid velocities in the mushy zone, and suppression of liquid velocities in solid regions, the sink term $\mathbf{F}_{\mathrm{d}}$ based on the enthalpy-porosity technique [52], was incorporated into the momentum equation and is defined as

$$\mathbf{F}_{\mathrm{d}} = C\, \frac{(1-\psi)^2}{\psi^3 + \epsilon}\, \mathbf{u}, \tag{8}$$

where C is the mushy-zone constant and its value was chosen to equal 10^7 kg m^{-2} s^{-2}, in accordance with [53] to avoid numerical artefacts associated with inappropriate assignment of this parameter, and ε is a constant equal to 10^{-3} employed to avoid division by zero.

To apply forces on the gas-metal interface, the continuum surface force (CSF) model [54] was employed. In the CSF model, surface forces are considered as volumetric forces acting on the material contained in grid cells in the interface region. The source term $\mathbf{F}_{\mathrm{s}}$ was added to (2) as follows:

$$\mathbf{F}_{\mathrm{s}} = \mathbf{f}_{\mathrm{s}} \|\nabla \phi\| \frac{2\rho}{\rho_{\mathrm{m}} + \rho_{\mathrm{g}}}, \tag{9}$$

where the surface force applied to a unit area $\mathbf{f}_{\mathrm{s}}$ comprises arc plasma, surface tension and Marangoni forces and was defined as follows:

$$\mathbf{f}_{\mathrm{s}} = \mathbf{f}_{\mathrm{a}} + \gamma \kappa \hat{\mathbf{n}} + \frac{\mathrm{d}\gamma}{\mathrm{d}T} \left[\nabla T - \hat{\mathbf{n}}\left(\hat{\mathbf{n}} \cdot \nabla T\right)\right], \tag{10}$$

where $\mathbf{f}_{\mathrm{a}}$ is arc plasma force, γ the surface tension, $\hat{\mathbf{n}}$ the surface unit normal vector ($\hat{\mathbf{n}} = \nabla\phi / \|\nabla\phi\|$) and κ the surface curvature ($\kappa = \nabla \cdot \hat{\mathbf{n}}$).

The arc plasma force $\mathbf{f}_{\mathrm{a}}$ defined in (10) comprises arc plasma shear stress $\mathbf{f}_{\tau}$ and arc pressure $\mathbf{f}_{\mathrm{p}}$,

$$\mathbf{f}_{\mathrm{s}} = \mathbf{f}_{\tau} + \mathbf{f}_{\mathrm{p}}. \tag{11}$$

the arc plasma shear stress $\mathbf{f}_{\tau}$, which applies tangent to the surface, was defined as follows [55]:

$$\mathbf{f}_{\tau} = \left[\tau_{\max}\, g_{\tau}\left(\mathscr{R}, \sigma_{\tau}\right)\right] \hat{\mathbf{t}}, \tag{12}$$

where the maximum arc shear stress $\tau_{\max}$ [56, 57], the arc shear stress distribution function g_τ [58] and the surface unit tangent vector $\hat{\mathbf{t}}$ [55] were defined as follows:

$$\tau_{\max} = 7\times10^{-2} I^{1.5} \exp\left(\frac{-2.5\times10^{4}\bar{\ell}}{I^{0.985}}\right), \tag{13}$$

$$g_\tau\left(\mathscr{R},\sigma_\tau\right) = \sqrt{\frac{\mathscr{R}}{\sigma_\tau}}\exp\left(\frac{-\mathscr{R}^2}{{\sigma_\tau}^2}\right), \tag{14}$$

$$\hat{\mathbf{t}} = \frac{\mathbf{r}-\hat{\mathbf{n}}\left(\hat{\mathbf{n}}\cdot\mathbf{r}\right)}{\left\|\mathbf{r}-\hat{\mathbf{n}}\left(\hat{\mathbf{n}}\cdot\mathbf{r}\right)\right\|}. \tag{15}$$

Here, I is the welding current in Amperes, $\bar{\ell}$ is the mean arc length in meters, $\mathscr{R}$ the radius in x-y plane (i.e. $\mathscr{R}=\sqrt{x^2+y^2}$) in meters, and $\mathbf{r}$ the position vector in the x-y plane in meters. The distribution parameter σ_τ (in meters) is assumed to be a function of the mean arc length $\bar{\ell}$ and current I and was approximated on the basis of the data reported by Lee and Na [56]:

$$\sigma_\tau = 1.387\times10^{-3} + I^{-0.595}\bar{\ell}^{0.733}. \tag{16}$$

the arc pressure $\mathbf{f}_\mathrm{p}$ was determined as follows [48]:

$$\mathbf{f}_\mathrm{p} = \mathscr{F}_\mathrm{p}\left[\frac{\mu_0 I}{4\pi}\frac{I}{2\pi{\sigma_\mathrm{p}}^2}\exp\left(\frac{-\mathscr{R}^2}{2{\sigma_\mathrm{p}}^2}\right)\right]\hat{\mathbf{n}}, \tag{17}$$

where I is the current in Amperes, and μ_0 is the vacuum permeability equal to $4\pi\times10^{-7}\ \mathrm{H\,m^{-1}}$. The distribution parameter σ_p (in metres) was determined using the experimental data reported by Tsai and Eagar [47] for an argon arc with an electrode tip angle of 75° as follows:

$$\sigma_\mathrm{p} = 7.03\times10^{-2}\ell^{0.823} + 2.04\times10^{-4}I^{0.376}, \tag{18}$$

where ℓ is the local arc length in meters, and I the current in Amperes. Hence, spatial and temporal variations of the arc pressure distribution resulted from changes in morphology of the melt-pool surface were taken into account. Changes in surface morphology can cause the total arc force applied to the melt-pool surface ($\iiint_\forall \|\mathbf{f}_\mathrm{p}\|\,\mathrm{d}V$) to differ from the expected arc force ($\mu_0 I^2/4\pi$) due to changes in $\|\nabla\phi\|$ [18, 59]. This numerical artefact was negated by incorporating $\mathscr{F}_\mathrm{p}$, which is defined as follows:

$$\mathscr{F}_\mathrm{p} = \alpha\frac{\mu_0 I^2}{4\pi}\frac{1}{\iiint_\forall \|\mathbf{f}_\mathrm{p}\|\,\mathrm{d}V}. \tag{19}$$

the dimensionless factor α was employed, as suggested by Liu *et al* [33] and Lin and Eagar [48], to match the theoretically determined arc pressure with experimentally measured values, and was calculated as follows:

$$\alpha = 3 + 8\times10^{-3}I, \tag{20}$$

with I the welding current in Amperes.

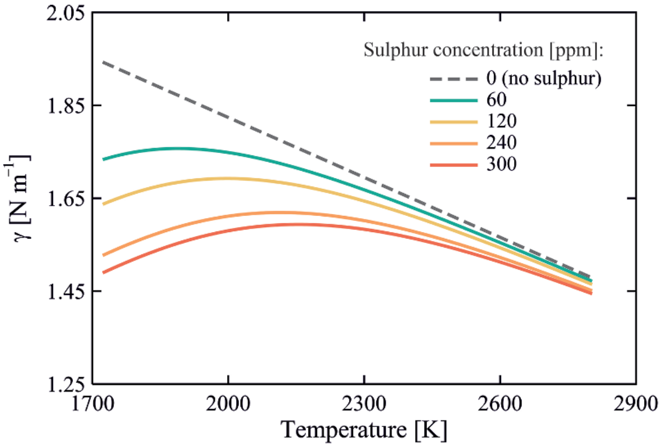

Figure 2. Surface tension of a molten Fe–S alloy as a function of temperature approximated using (21) for different sulphur concentrations.

The temperature-dependent surface tension of the molten material was modelled using an empirical correlation [41] that accounts for the influence of sulphur as a surface-active element, and is defined as follows:

$$\gamma = \gamma_\mathrm{m}^\circ + \left(\frac{\partial\gamma}{\partial T}\right)^\circ\left(T-T_\mathrm{m}\right) - \mathrm{R}T\Gamma_\mathrm{s}\ln\left[1+\psi a_\mathrm{s}\exp\left(\frac{-\Delta H^\circ}{\mathrm{R}T}\right)\right], \tag{21}$$

where γ_m° is the surface tension of the pure molten-material at the melting temperature T_m, $(\partial\gamma/\partial T)^\circ$ the temperature gradient of the surface tension of the pure molten-material, T the temperature in Kelvin, Γ_s the adsorption at saturation, R the universal gas constant, ψ an entropy factor, a_s the activity of the solute, and ΔH° the standard heat of adsorption. The values reported by Sahoo *et al* [41] were used for the properties in (21). Variations of the surface tension of a molten Fe–S alloy with temperature are shown in figure 2 for different sulphur concentrations studied in the present work. It should be noted that in this model it is assumed that sulphur is distributed uniformly over the melt-pool surface. Since temperatures in the melt-pool are below the boiling temperature of stainless steel ($\mathscr{O}(3000\ \mathrm{K})$) and there is no material addition with a different sulphur concentration, the effects of changes in the sulphur concentration is virtually negligible for the cases studied in the present work. Therefore, the effects of adsorption, desorption and redistribution of species along the melt-pool surface are neglected in the present numerical simulations.

$\mathbf{F}_\mathrm{b}$ in (2) is the body force, which comprises electromagnetic, gravity and thermal buoyancy forces. The electromagnetic force was computed using the model proposed by Tsao and Wu [60] transformed into a body-fitted coordinate system, and the thermal buoyancy force was modelled using the Boussinesq approximation [61]. Hence, the body forces are defined as follows:

$$\mathbf{f}_{\mathrm{b}x} = \frac{-\mu_0 I^2}{4\pi^2 \sigma_{\mathrm{e}}{}^2 \mathscr{R}} \exp\left(\frac{-\mathscr{R}^2}{2\sigma_{\mathrm{e}}{}^2}\right)\left[1 - \exp\left(\frac{-\mathscr{R}^2}{2\sigma_{\mathrm{e}}{}^2}\right)\right] \times \left(1 - \frac{z - z'}{H_{\mathrm{m}} - z'}\right)^2 \left(\frac{x}{\mathscr{R}}\right), \tag{22}$$

$$\mathbf{f}_{\mathrm{b}y} = \frac{-\mu_0 I^2}{4\pi^2 \sigma_{\mathrm{e}}{}^2 \mathscr{R}} \exp\left(\frac{-\mathscr{R}^2}{2\sigma_{\mathrm{e}}{}^2}\right)\left[1 - \exp\left(\frac{-\mathscr{R}^2}{2\sigma_{\mathrm{e}}{}^2}\right)\right] \times \left(1 - \frac{z - z'}{H_{\mathrm{m}} - z'}\right)^2 \left(\frac{y}{\mathscr{R}}\right), \tag{23}$$

$$\mathbf{f}_{\mathrm{b}z} = \frac{-\mu_0 I^2}{4\pi^2 \sigma_{\mathrm{e}}{}^2 \mathscr{R}} \exp\left(\frac{-\mathscr{R}^2}{2\sigma_{\mathrm{e}}{}^2}\right)\left(1 - \frac{z - z'}{H_{\mathrm{m}} - z'}\right) + \rho\mathbf{g} - \rho\beta\left(T - T_{\mathrm{l}}\right)\mathbf{g}. \tag{24}$$

Here, the distribution parameter for the electromagnetic force σ_{e} is the same as σ_{p}, according to Tsai and Eagar [47], z' is the position of the melt-pool surface in x-y plane, β the thermal expansion coefficient, and $\mathbf{g}$ the gravitational acceleration vector.

The thermal energy provided by the arc was modelled by adding the source term S_{q} to the energy equation (3) and was defined as

$$S_{\mathrm{q}} = \mathscr{F}_{\mathrm{q}}\left[\frac{\eta IU}{2\pi\sigma_{\mathrm{q}}{}^2} \exp\left(\frac{-\mathscr{R}^2}{2\sigma_{\mathrm{q}}{}^2}\right)\|\nabla\phi\| \frac{2\rho c_{\mathrm{p}}}{(\rho c_{\mathrm{p}})_{\mathrm{m}} + (\rho c_{\mathrm{p}})_{\mathrm{g}}}\right], \tag{25}$$

where the process efficiency η considered to be a linear function of welding current, varying from 80% at 50 A to 70% at 300 A [62]. It should be noted that the source term S_{q} is only applied to the top surface of the workpiece. The arc voltage U depends on welding current and arc length, and was determined as follows:

$$U = U_{\mathrm{o}} + U_{\mathrm{I}} I + U_{\mathrm{e}}\bar{\ell}, \tag{26}$$

where U_{o} is the electrode fall voltage equal to 8 V [63], U_{I} the coefficient of variation of arc voltage with current equal to 1.3×10^{-2} V A^{-1} [64], and U_{e} the electric field strength equal to 7.5 V cm^{-1} [63]. Using the data reported by Tsai and Eagar [47], the distribution parameter σ_{q} (in meters) was determined as follows:

$$\sigma_{\mathrm{q}} = 1.61 \times 10^{-1} \ell^{0.976} + 2.23 \times 10^{-4} I^{0.395}, \tag{27}$$

with ℓ in meters and I in Amperes. The adjustment factor $\mathscr{F}_{\mathrm{q}}$ was used to negate changes in the total heat input due to surface deformations, which is defined as follows:

$$\mathscr{F}_{\mathrm{q}} = \frac{\eta IU}{\iiint_{\forall} S_{\mathrm{q}}\,\mathrm{d}V}. \tag{28}$$

the sink term S_{l} was added to the energy equation to account for heat losses due to convection and radiation, and was determined as follows:

$$S_{\mathrm{l}} = -\left[\mathscr{h}_{\mathrm{c}}\left(T - T_0\right) + \mathscr{K}_{\mathrm{b}}\mathscr{E}\left(T^4 - T_0{}^4\right)\right] \times \|\nabla\phi\| \frac{2\rho c_{\mathrm{p}}}{(\rho c_{\mathrm{p}})_{\mathrm{m}} + (\rho c_{\mathrm{p}})_{\mathrm{g}}}, \tag{29}$$

where $\mathscr{h}_{\mathrm{c}}$ is the heat transfer coefficient equal to 25 W m^{-2} K^{-1} [65], $\mathscr{K}_{\mathrm{b}}$ the Stefan–Boltzmann constant and $\mathscr{E}$ the radiation emissivity equal to 0.45 [66].

3.2. *Numerical implementation*

The numerical simulations reported in the present work make use of a finite-volume solver, ANSYS Fluent [67]. The surface-tension model as well as the source terms in the governing equations were implemented in the solver using user-defined functions programmed in the C programming language. The computational grid contains about 5.2×10^6 hexahedral cells, where cell spacing varies gradually from 40 μm in the melt-pool region and close to the gas-metal interface to 400 μm close to the boundaries of the computational domain. Spatial discretisation was implemented by the central-differencing scheme for momentum advection and diffusive fluxes, and the time marching was performed employing a first order implicit scheme. The time-step size was set to 10^{-5} s, resulting in a Courant number ($\mathrm{Co} = \|\mathbf{u}\|\Delta t/\Delta x$) less than 0.25. Velocity and pressure fields were coupled using the PISO (pressure-implicit with splitting of operators) scheme [68] and the pressure interpolation was performed employing the PRESTO (pressure staggering option) scheme [69]. The advection of the volume-fraction field was formulated using an explicit compressive VOF method [70]. Convergence for each time-step is achieved when scaled residuals fall below 10^{-7}. Each simulation was executed in parallel on 80 cores (AMD EPYC 7452) of a computing cluster for a total run-time of about 800 h. To reduce the computational costs associated with running the model, possible developments can focus on performing model order reduction or decreasing the spatial and temporal resolutions of the simulations. Reliability, validity and grid independence of the present numerical model in predicting internal flow behaviour, evolution of the melt-pool shape and surface oscillations were meticulously verified in our previous works [18, 53, 71, 72]. Moreover, the frequencies acquired from the present three-dimensional numerical simulations deviate less than 10% from the experimental data reported by Yudodibroto [73].

3.3. *Time-frequency analysis*

Because of the complex unsteady molten metal flow in the melt pool, the frequency spectra of signals received from an oscillating melt-pool during GTA welding are often time-variant. The dynamic features of the oscillation signals cannot be disclosed employing the conventional Fourier transform (FT) analysis [74]. The continuous wavelet transform (CWT) [75] was employed in the present study to overcome the shortcomings of the conventional fast Fourier transform (FFT) analysis in characterising the non-stationary features of the signals that may contain abrupt changes in their frequency

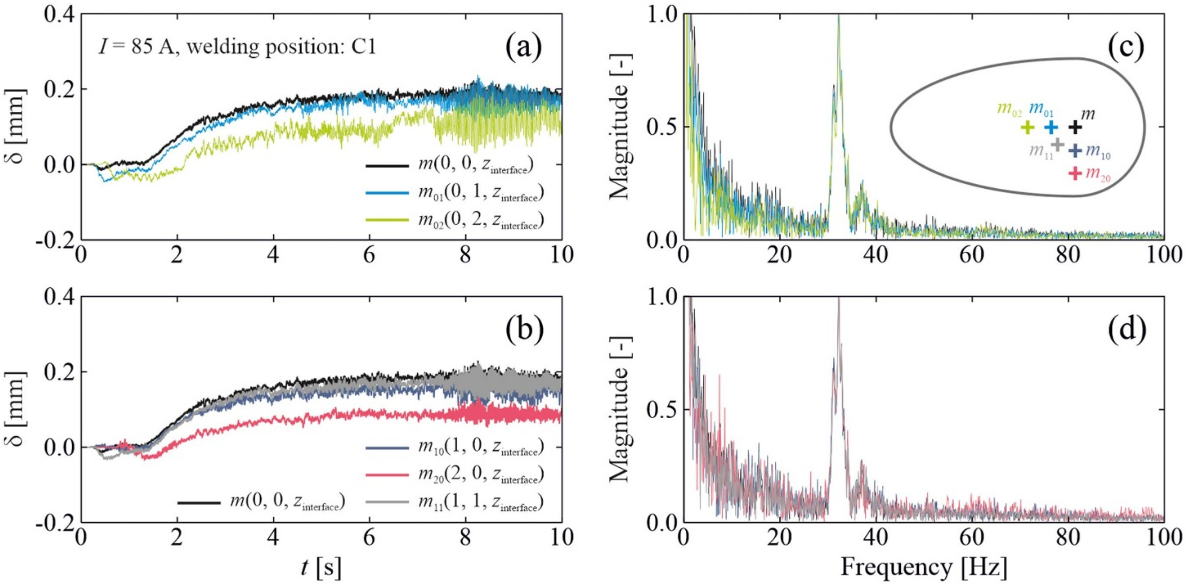

Figure 3. The displacement signals recorded from the monitoring points on the melt-pool top surface and the corresponding frequency spectra for welding position C1. (a) and (b) displacement signals obtained from the simulations, (c) and (d) frequency spectra obtained from FFT analysis. Magnitudes in frequency spectrum are normalised with respect to the maximum magnitude. Positive values of δ indicate surface depression and its negative values indicate surface elevation. ($I = 85$ A, travel speed: 2.5 mm s^{-1} and sulphur concentration: 240 ppm.)

spectra. Employing the CWT method, the time-resolved melt-pool surface oscillation signals obtained from the numerical simulations can be decomposed into time and frequency spaces simultaneously. The principle of signal processing based on the wavelet transform is described in [75] and is not repeated here. The Python programming language was employed to perform time-frequency analysis using the oscillation signals acquired at a sampling frequency of 10^5 Hz. The Morlet wavelet function, which is a Gaussian-windowed complex sinusoid, was used as the mother wavelet that yields an adequate balance in both time and frequency domains.

4. Results

In this section, the effects of different welding positions (shown in figure 1(c)) as well as travel speed (ranging between 1.25 mm s^{-1} and 5 mm s^{-1}) and sulphur concentration (ranging between 60 ppm and 300 ppm) on internal flow behaviour, evolution of the melt-pool shape and surface oscillations during GTA welding are described. Displacement signals required for characterising the molten metal oscillations were recorded from several monitoring points distributed over the melt-pool surface during the simulations, and are shown in figure 3 for welding position C1. Although the amplitudes of oscillations are different at different locations, the frequency spectra obtained from FFT analysis look similar. Hence, the signals recorded from the monitoring point $m(x, y, z) = m(0, 0, z_{\text{interface}})$ in the period of $t = 0$ to 10 s were analysed utilising the continuous wavelet transform. It should be noted that no triggering action (such as welding current pulsation) was taken to excite melt-pool surface oscillations in the present numerical simulations because even small surface fluctuations are detectable using the proposed computational approach [18]. The effects of triggering melt-pool oscillations through welding-current pulsation is studied for welding position C1, travel speed of 2.5 mm s^{-1} and sulphur concentration of 240 ppm, and the results are presented in the supplementary materials (available online at stacks.iop.org/JPD/54/275303/mmedia).

The oscillation signals of the melt-pool surface and the corresponding frequency spectra for different welding positions with $I = 85$ A and sulphur concentration of 240 ppm are shown in figure 4 for downward welding direction (C1–C4) and in figure 5 for upward welding direction (C5–C8). For the cases with a travel speed of 2.5 mm s^{-1}, the melt-pool depth increases over time and reaches the plate thickness H_{m} in about 1.25 s. Then, the melt-pool surface area on the bottom surface increases and becomes almost the same as that on the top surface (i.e. full penetration) at $t \approx 4$ s, after which the melt-pool grows to reach a quasi-steady state. In the case of GTA welding in position C1 (figure 4(a)), the frequency of oscillations decreases from $f \approx 73$ Hz at $t = 1.25$ s to values of about 32 Hz at $t = 4$ s, while the melt-pool surface area on the bottom surface is increasing to establish full penetration. After full penetration is established, the frequency of the most energetic event increases to $f \approx 45$ Hz, as indicated by arrow, and subsequently decreases gradually to values of about 32 Hz as time passes and reaches 10 s. Both low and high frequencies remain in the spectrum after full penetration. The amplitudes of oscillations also augment as the melt-pool size increases. The frequency of oscillations obtained from the present numerical simulations for welding position C1 agrees reasonably (within 10% deviation bands) with the experimental data reported

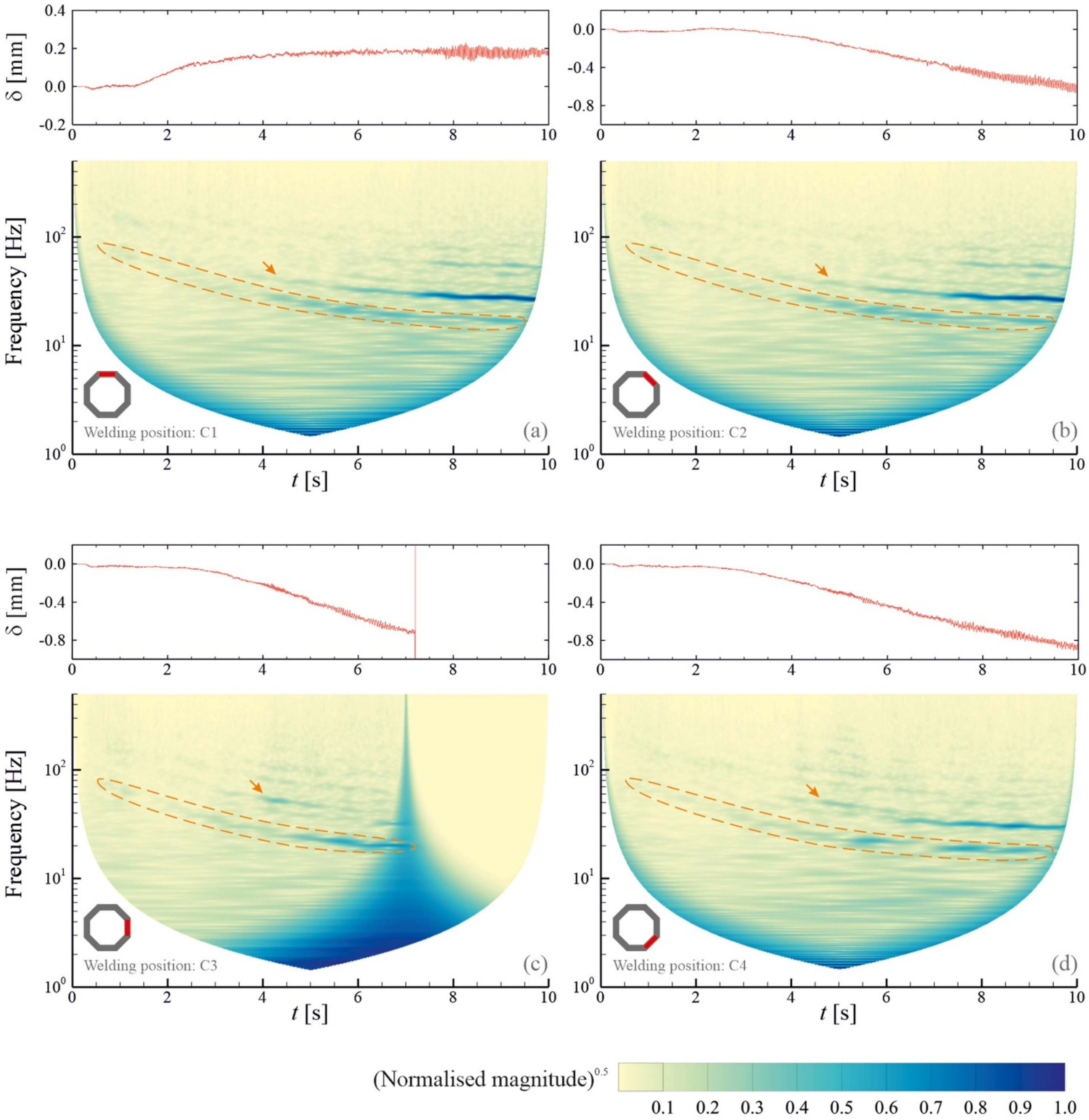

Figure 4. The displacement signals recorded from the monitoring point $m(x,y,z) = m(0,0,z_{\mathrm{interface}})$ and the corresponding time-frequency spectra for different welding positions with downward welding direction. (a) Welding positions C1, (b) welding positions C2, (c) welding positions C3 and (d) welding positions C4. Magnitudes are normalised with respect to the maximum magnitude in the time-frequency spectrum. Positive values of δ indicate surface depression and its negative values indicate surface elevation. ($I = 85$ A, travel speed: 2.5 $\mathrm{mm\,s^{-1}}$ and sulphur concentration: 240 ppm.)

by Li *et al* [76]. The range of oscillation frequencies predicted for different welding positions (C1–C8) seems to be the same, however the results suggest that the welding position affects the amplitudes of oscillations and the evolution of melt-pool oscillatory behaviour. The frequency of oscillations varies from $f \approx 25$ Hz to values of about 37 Hz after full penetration for welding positions C2 and C4. Such increase in the frequency of oscillations after full penetration also occurs for the welding position C3, however the frequency decreases after about 1 s and the melt pool oscillates at low frequencies up to $t \approx 7$ s, after which the melt pool collapses (i.e. burns-through).

The amplitude of oscillations predicted for cases C5–C8 are generally larger than those predicted for cases C1–C4, as shown in figure 5. For the welding position C5, the frequency of oscillations decreases from 66 to 52 Hz within 1 s (from $t = 1.25$ to $t = 2.25$ s) and then the frequency of oscillations increases to 64 Hz, as indicated by arrow. For the cases that welding direction is upward (C6–C8), multiple changes occur in the frequency of oscillations. The abrupt changes observed in the frequency domain indicate the importance of utilising the wavelet transform instead of the Fourier transform for analysing the behaviour of oscillating melt-pools. Changes in the frequency of oscillations relate to changes in flow pattern in

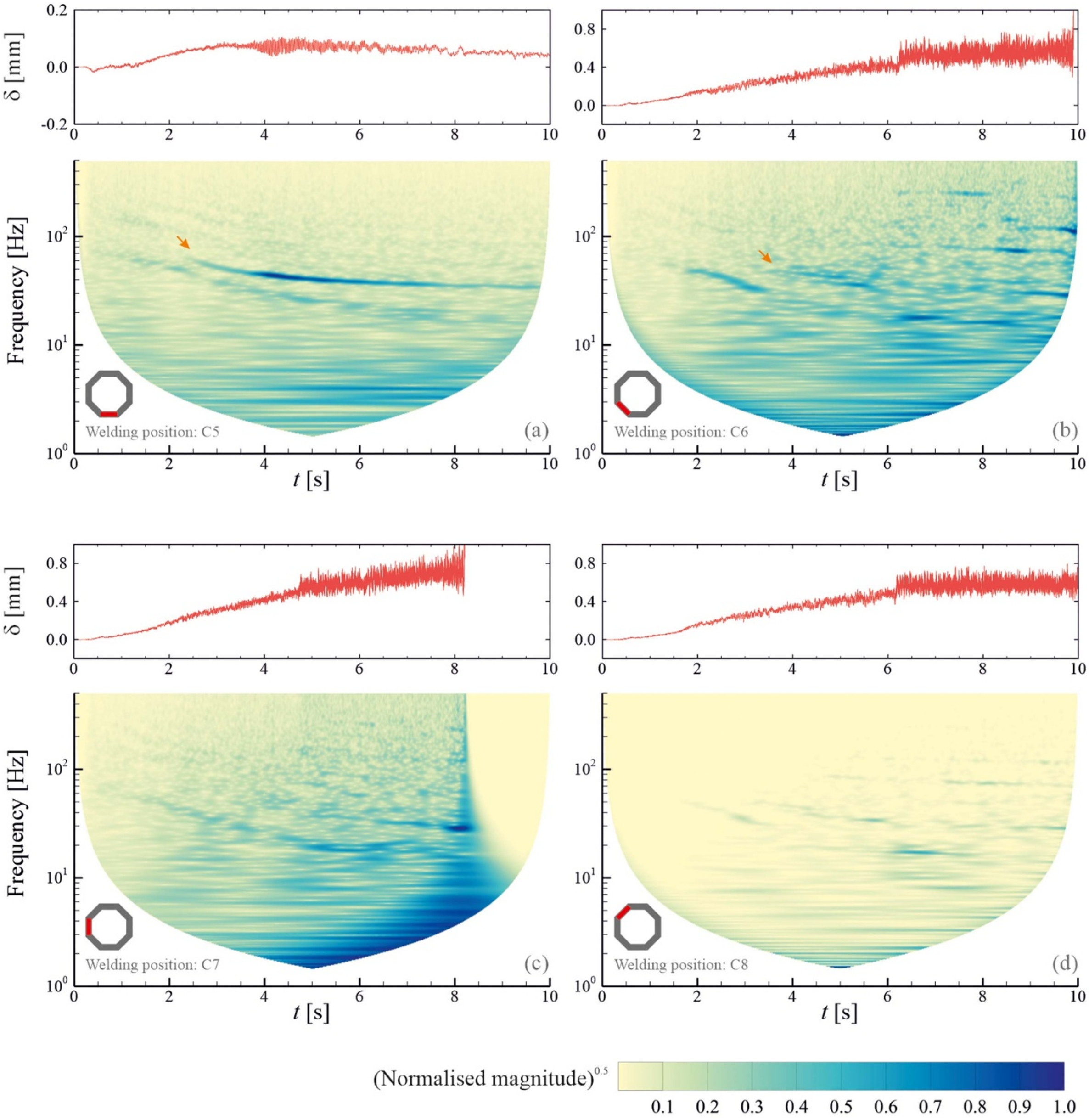

Figure 5. The displacement signals recorded from the monitoring point $m(x,y,z)=m(0,0,z_{\text{interface}})$ and the corresponding time-frequency spectrum for different welding positions with upward welding direction. (a) Welding positions C5, (b) welding positions C6, (c) welding positions C7 and (d) welding positions C8. Magnitudes are normalised with respect to the maximum magnitude in the time-frequency spectrum. Positive values of δ indicate surface depression and its negative values indicate surface elevation. ($I=85$ A, travel speed: 2.5 mm s^{-1} and sulphur concentration: 240 ppm.)

the melt pool, the shape and size of the melt-pool, and surface tension of the molten metal [14, 18], which is discussed in section 5.

Changes in the sulphur concentration of the material, as a surface-active element, can result in notable changes in surface tension of the molten material and its variation with temperature ($\partial\gamma/\partial T$), as shown in figure 2. Reducing the amount of sulphur in the material results in intensifying the outward fluid flow over the melt-pool surface (as shown in figure 11), forming a wide melt pool. The effect of sulphur concentration of the material on the evolution of the frequency of oscillations is shown in figure 6 for welds in position C1 and travel speed of 2.5 mm s^{-1}. The evolution of oscillation frequency is almost the same for the cases with sulphur concentrations of 120 and 60 ppm, and differs both qualitatively and quantitatively from that of the case containing 240 ppm sulphur. The melt pool oscillates at higher frequencies with larger amplitudes in the case with sulphur concentration of 240 ppm compared to the cases with sulphur concentrations of 120 and 60 ppm. Moreover, the fundamental frequency of oscillations does not increase markedly after full penetration in the cases with sulphur concentrations of 120 and 60 ppm, as it does in the case with sulphur concentration of 240 ppm. This difference in the evolution of oscillations frequency relates to changes in the structure of the molten metal flow in the melt pool and thus melt-pool shape evolution.

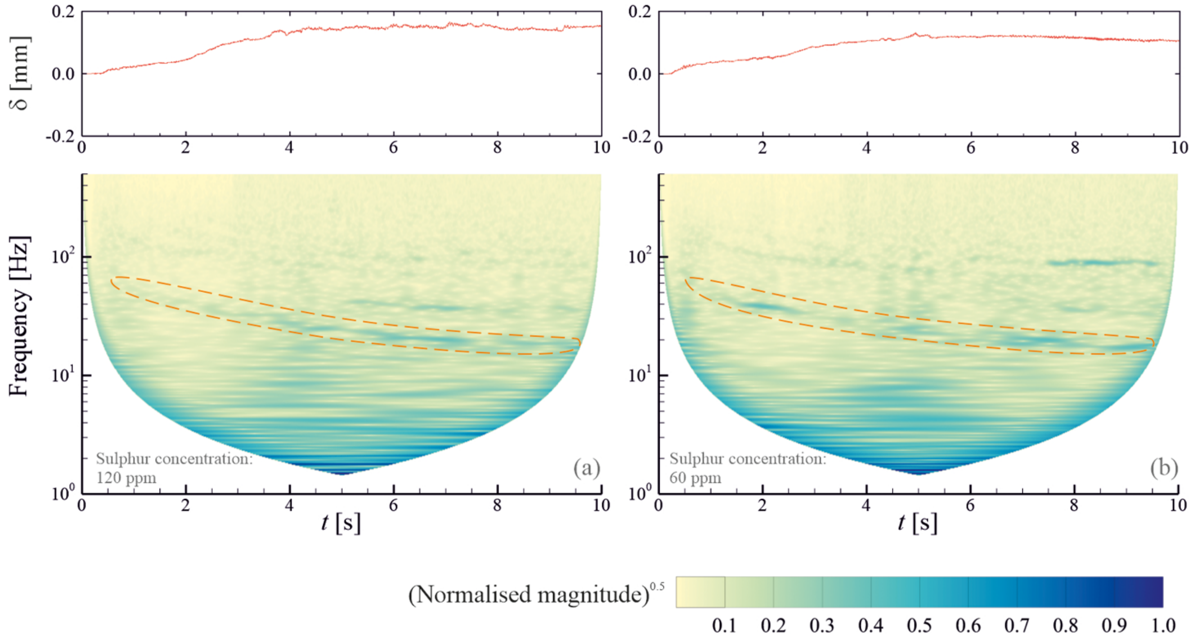

Figure 6. The influence of sulphur concentration on the time-frequency spectra of melt-pool oscillations during GTA welding. (a) Sulphur concentration: 120 ppm, and (b) sulphur concentration: 60 ppm magnitudes are normalised with respect to the maximum magnitude in the time-frequency spectrum. Positive values of δ indicate surface depression and its negative values indicate surface elevation. ($I = 85$ A, welding position: C1 and travel speed: 2.5 mm s^{-1}.)

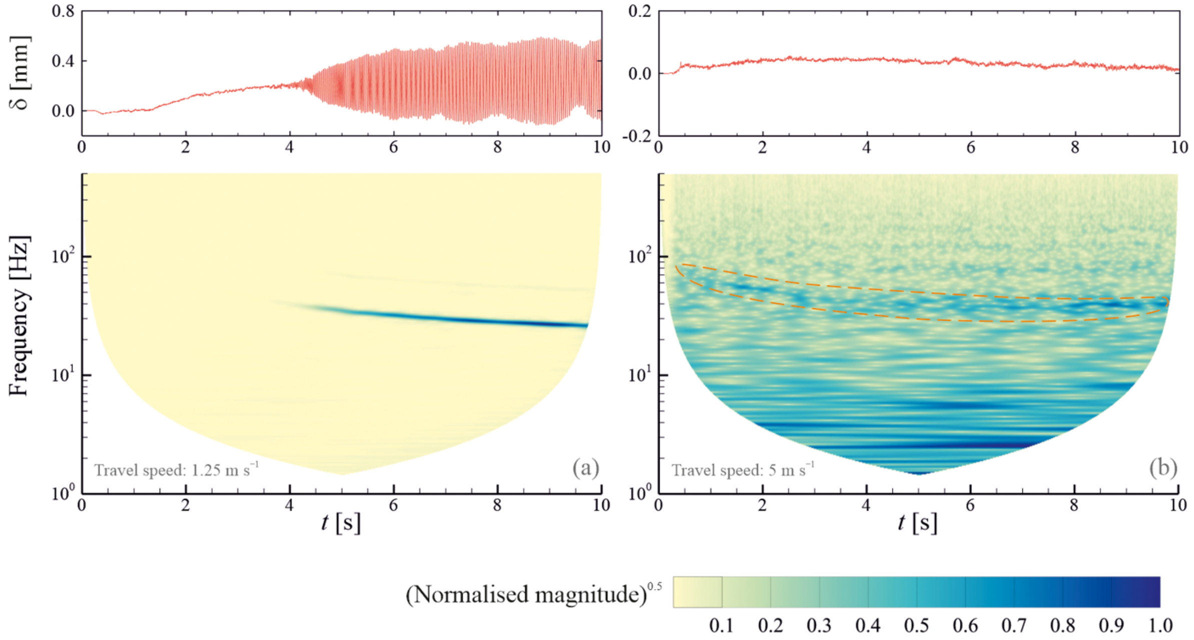

Figure 7. The influence of welding travel speed on the time-frequency spectra of melt-pool oscillations during GTA welding. (a) Travel speed: 1.25 mm s^{-1} and (b) travel speed: 5 mm s^{-1}. Magnitudes are normalised with respect to the maximum magnitude in the time-frequency spectrum. Positive values of δ indicate surface depression and its negative values indicate surface elevation. ($I = 85$ A, welding position: C1 and sulphur concentration: 240 ppm.)

The influence of travel speed on the frequency of melt-pool surface oscillations is shown in figure 7 for the welds in position C1 and sulphur concentration of 240 ppm. When the travel speed was set to 1.25 mm s^{-1}, the melt pool reaches full penetration at $t \approx 3$ s and the amplitude of surface oscillations start to increase, as shown in figure 7(a). For the case with a travel speed of 1.25 mm s^{-1}, the frequency of oscillations gradually decreases from 69 Hz at $t = 1.25$ s to 29 Hz at $t = 10$ s while the melt-pool is growing over time. Increasing the travel speed from 1.25 to 5 mm s^{-1}, the amplitude of oscillations decreases significantly. Moreover, the frequency of oscillations decreases up to $t = 4$ s while the melt-pool

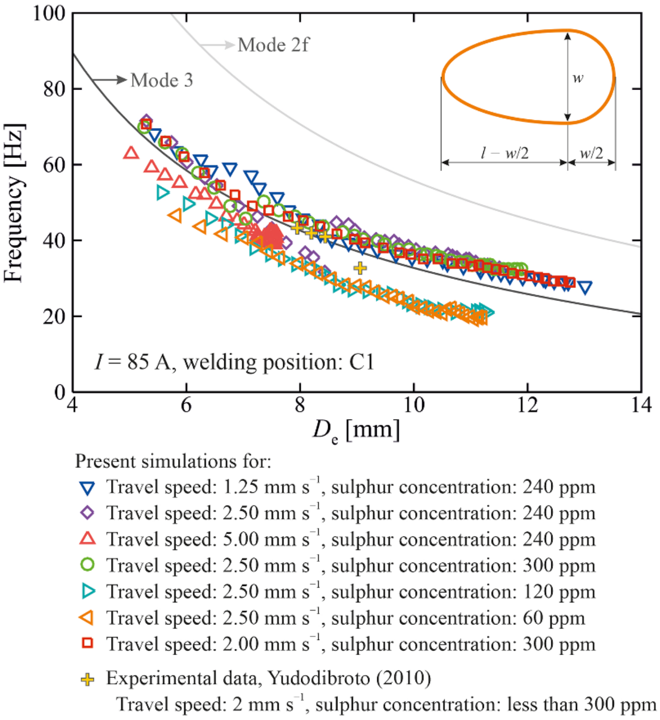

Figure 8. Variation of the frequency of oscillations for fully-penetrated melt-pools during GTA welding as a function of equivalent melt-pool diameter. The frequency of oscillations obtained from the present numerical simulations (unfilled symbols), experimental data reported by Yudodibroto [73] (plus symbols), and analytical approximations using the model proposed by Maruo and Hirata [16] for oscillation frequencies in Mode 3 (up and down bulk motion, dark grey line) and Mode 2f (sloshy oscillation, light grey line). ($I = 85$ A and welding position: C1.)

size is increasing. Afterwards, the melt-pool reaches a quasi-steady-state condition and the variation of the melt-pool size over time becomes insignificant, resulting surface oscillations at an almost constant frequency of about 41 Hz. It should be noted that when the pool size has reached steady state, the surface area of the melt pool on the bottom surface is consistently smaller than that on the top-surface in the case with a travel speed of 5 mm s^{-1}.

5. Discussion

The frequency of oscillations predicted using the present numerical simulations are compared to the analytical approximations calculated from the model developed by Maruo and Hirata [16] for fully-penetrated melt pools in welding position C1, and the results are presented in figure 8. This analytical model is expressed mathematically as follows [16]:

$$f = \frac{1}{2\pi}\sqrt{\frac{2\bar{\gamma}\kappa^2}{\rho H_\mathrm{m}} - \frac{2\|\mathbf{g}\|}{H_\mathrm{m}}}, \tag{30}$$

where H_m is the plate thickness, ρ the density of the molten metal and $\bar{\gamma}$ the average surface tension of the molten material. The mean value of surface tension for the alloy considered in the present study is approximately 1.6 N m^{-1} in the temperature range of 1723 K–2500 K [41]. The value of κ in (30) depends on both melt-pool size and oscillation mode and is obtained from the following equations [73]:

$$\text{Mode 3: } \kappa = 2.405\left(\frac{D_\mathrm{e}}{2}\right)^{-1}, \tag{31}$$

$$\text{Mode 2f: } \kappa = 3.832\left(\frac{D_\mathrm{e}}{2}\right)^{-1}, \tag{32}$$

where D_e is the equivalent diameter of the melt-pool under full penetration condition defined as follows:

$$D_\mathrm{e} = \sqrt{lw}, \tag{33}$$

where l and w are the melt-pool length and width on the top surface respectively, as shown in figure 8. The analytical model of Maruo and Hirata [16] is developed for fully-penetrated melt pools, assuming that the melt-pool shape and size on the top and bottom surfaces of the workpiece are the same with no offset. It appears that for the case with a travel speed of 2.5 mm s^{-1} and sulphur concentration of 240 ppm the melt-pool surface oscillations follow the analytically predicted frequencies in mode 3 for $t > 4$ s when the surface area of the melt-pool on the bottom surface approaches the surface area on the top surface. Reducing travel speed to 1.25 mm s^{-1} while keeping the sulphur concentration unchanged (240 ppm), the melt-pool surface area on the bottom surface becomes almost the same as on the top surface and the predicted frequencies follow the analytical predictions in mode 3. For the case with a travel speed of 5 mm s^{-1} and sulphur concentration of 240 ppm, the melt pool shape and size reach a quasi-steady-state with an equivalent diameter $D_\mathrm{e} \approx 7.5$ mm that does not change notably over time. In many practical applications, the melt-pool surface area is not necessarily the same on the top and bottom surfaces of the workpiece, particularly when the melt pool is growing before reaching a quasi-steady-state. Moreover, there is often an offset between the positions of the melt-pool surfaces on the top and bottom of the workpiece, which increases with increasing the travel speed. These differences in the melt-pool size and shape, as well as the offset between the melt-pool surfaces on the top and bottom surfaces of the workpiece, lead to deviation of the frequencies approximated using the analytical models from those predicted from numerical simulations and measured experimentally. The frequencies predicted using the present numerical simulations are in reasonably good agreement (within 10% deviation bands) with the experimental measurements of fully penetrated pools reported by Yudodibroto [73].

Despite the suitability of analytical models for predicting the frequency of oscillations under a full penetration condition, they fail to predict changes in oscillation mode during welding processes, particularly when the melt pool is evolving over time. Moreover, variation in the value of surface tension of the molten material with temperature is ignored in the analytical models, which limits their accuracy in predicting

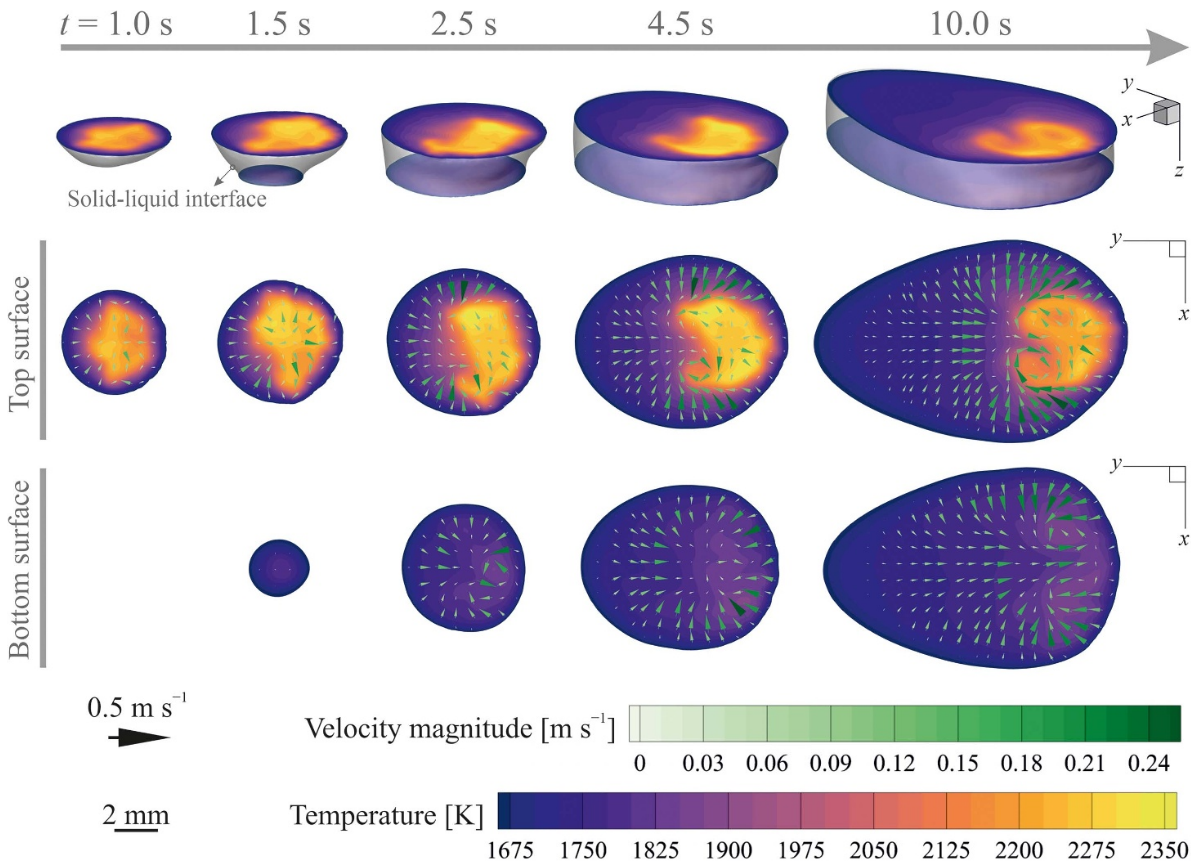

Figure 9. Evolution of the melt-pool shape during gas tungsten arc welding. Contours show the temperature distribution over the melt-pool surface and are overlaid with velocity vectors. The 0.5 m s^{-1} reference vector is provided for scaling the velocity field. ($I = 85$ A, welding position: C1, travel speed: 2.5 mm s^{-1} and sulphur concentration: 240 ppm.)

the frequency of oscillations during GTA welding. The results presented in figure 8 also demonstrate that changes in the sulphur concentration can affect the frequency of oscillations and their evolution due to variations in the internal flow pattern and thus the melt-pool shape, which results from changes in the Marangoni stresses acting on the melt-pool surfaces.

Figure 9 shows the evolution of the thermal and flow fields over the melt-pool surfaces as well as the pool shape during GTA welding in position C1 with a travel speed of 2.5 mm s^{-1} and sulphur concentration of 240 ppm. A melt pool forms soon after the arc ignition, grows and its depth reaches the plate thickness after about 1.25 s, forming a fully-penetrated melt pool. Fluid flow in the melt pool is driven by various time-variant forces acting on the molten material such as Marangoni, Lorentz, arc plasma shear and pressure and buoyancy forces, resulting in a complex flow pattern that is inherently three-dimensional. This fluid motion transfers the heat absorbed by the material and affects the melt-pool shape and its evolution over time. The relative contribution of advective to diffusive energy transfer can be evaluated using the Péclet number ($\mathrm{Pe} = \rho c_\mathrm{p} \mathscr{D} \|\mathbf{u}\| / k$), which is larger than unity ($\mathcal{O}(100)$) for the cases studied in the present work, signifying the notable influence of advection on the melt-pool shape.

The results shown in figure 9 indicate that the maximum temperature of the melt pool after reaching a quasi-steady-state condition varies between 2260 K and 2340 K and the maximum local fluid velocity varies between 0.21 and 0.34 m s^{-1}. Inward fluid flow from the boundary to the centre of the pool is observed over the top surface that meets an outward flow in the central region. This change in the flow direction is due to the sign change of the temperature gradient of surface tension ($\partial\gamma/\partial T$) at a specific temperature, as shown in figure 2. Interactions between these two streams disturb the thermal field over the pool surface and generate an unsteady complex flow pattern inside the pool, affecting the energy transport in the melt pool and thus the evolution of the melt-pool shape. Temperatures are below the critical temperature over the bottom surface of the pool and the temperature gradient of the surface tension is positive all over the surface, resulting in inward fluid flow from the melt-pool boundaries. Moreover, two vortices form over the top surface as time passes that generate a periodic asymmetry in the flow field, leading to flow oscillations around the melt-pool centreline. The formation of such vortices occurs because of the fluid motion from the front part of the pool toward the rear and collision with the inward flow in the rear part of the pool. A similar flow pattern was observed during GTA welding by Zhao *et al* [43] using particle image velocimetry (PIV).

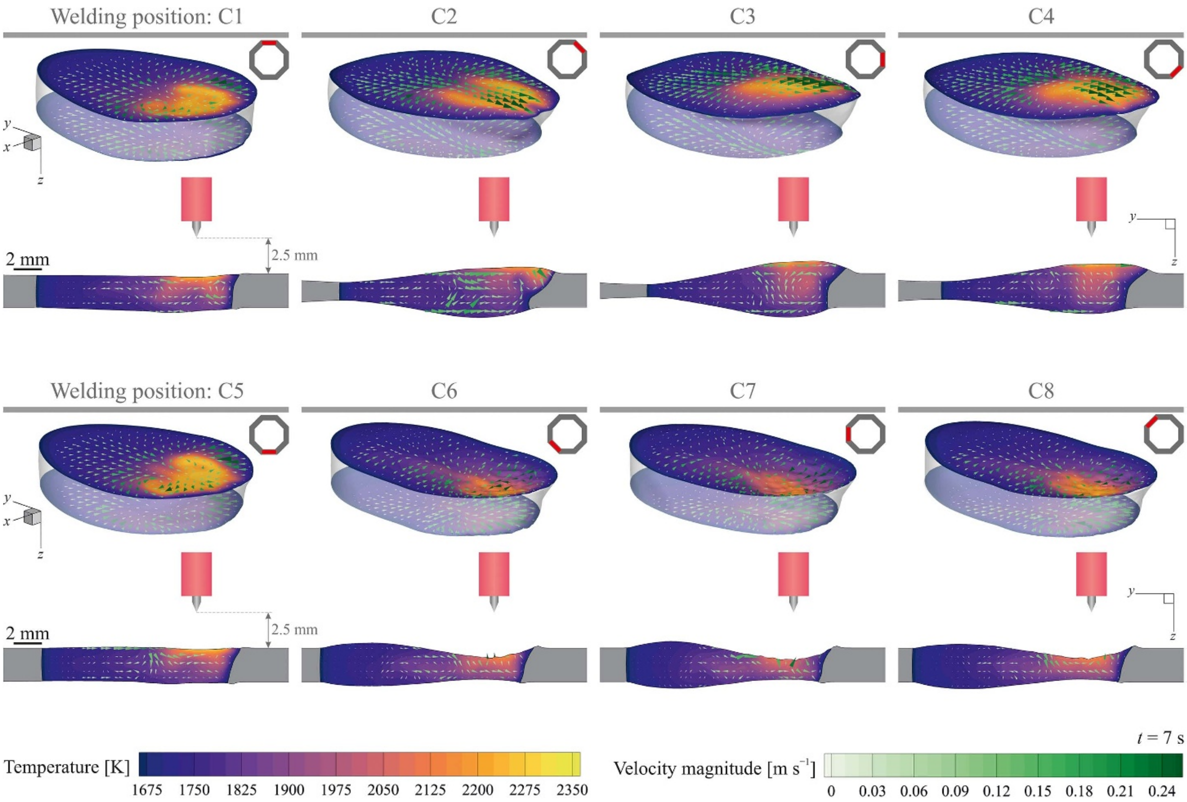

Figure 10. The influence of the welding position on evolution of the melt-pool shape during gas tungsten arc welding. Contours show the temperature profile at $t = 7$ s and are overlaid with velocity vectors. Cross sections on the y-z plane are located at $x = 0$. ($I = 85$ A, travel speed: 2.5 mm s^{-1} and sulphur concentration: 240 ppm.)

The outward fluid flow in the central region of the melt pool coupled with the arc pressure applied to the molten material leads to melt-pool surface depressions in the front and central region of the melt pool. Variation in the flow pattern over time, as well as changes in the melt-pool shape result in changes in oscillatory behaviour. For the case shown in figure 9, the melt-pool surface area on the bottom surface of the workpiece increases over time and becomes almost the same as that on the top surface after 4 s. This change in pool shape coupled with the fluid flow that evolves over the bottom surface, causes a change in the melt-pool oscillatory behaviour, as reflected in figure 4. Variations in the pool surface morphology also result in variation of the power-density and arc force distribution over the surface and the total power input from the electric arc, enhancing flow disturbances.

Variation in the welding position can affect melt-pool surface deformations, resulting in changes in the power-density and arc force distribution over the melt-pool surface and thus the evolution of the melt-pool shape and its oscillatory behaviour. The influence of welding position on melt-pool shape is shown in figure 10 for cases with a travel speed of 2.5 mm s^{-1} and sulphur concentration of 240 ppm. When welding downward (C2–C4), the molten material is pulled by the gravitational force towards the front part of the melt pool and forms a bulge beneath the welding torch. This change in the melt-pool surface morphology decreases the average arc length and alters the power-density distribution, through changing the distribution parameter σ_q (27), and thus temperature profile over the surface. The change in the power-density distribution in turn increases the temperature gradients over the melt-pool surface and thus the magnitude of Marangoni forces. The results reveal that the molten material moves from the rear of the melt pool towards the front around the centreline, resulting in further reduction of the melt-pool thickness in the rear part of the melt pool, which can eventually lead to the rupture of liquid layer and melt-pool collapse if the dynamic force balance cannot be maintained. In contrast, when welding upward (C6–C8), the molten material moves towards the rear part of the melt pool because of the gravitational force, forming a concavity in the front part of the pool. The formation of this concavity increases the average arc length beneath the welding torch and the distribution parameter σ_q (27). This increase in the distribution parameter reduces the temperature gradients over the melt pool surface and thus the magnitude of Marangoni forces. These results suggest that although the melt-pool shape and its surface morphology are influenced by the welding position, the overall flow structure in the melt pool, which is dominated by Marangoni and electromagnetic forces, is not affected significantly by the gravitational force [46]. The results in figure 10 also show that the material thickness H reduces locally beneath the welding torch with the increase in the average arc length in the cases that welding direction is upward (C6–C8). This reduction in the material thickness results in the establishment of full penetration somewhat earlier at $t \approx 3$ s

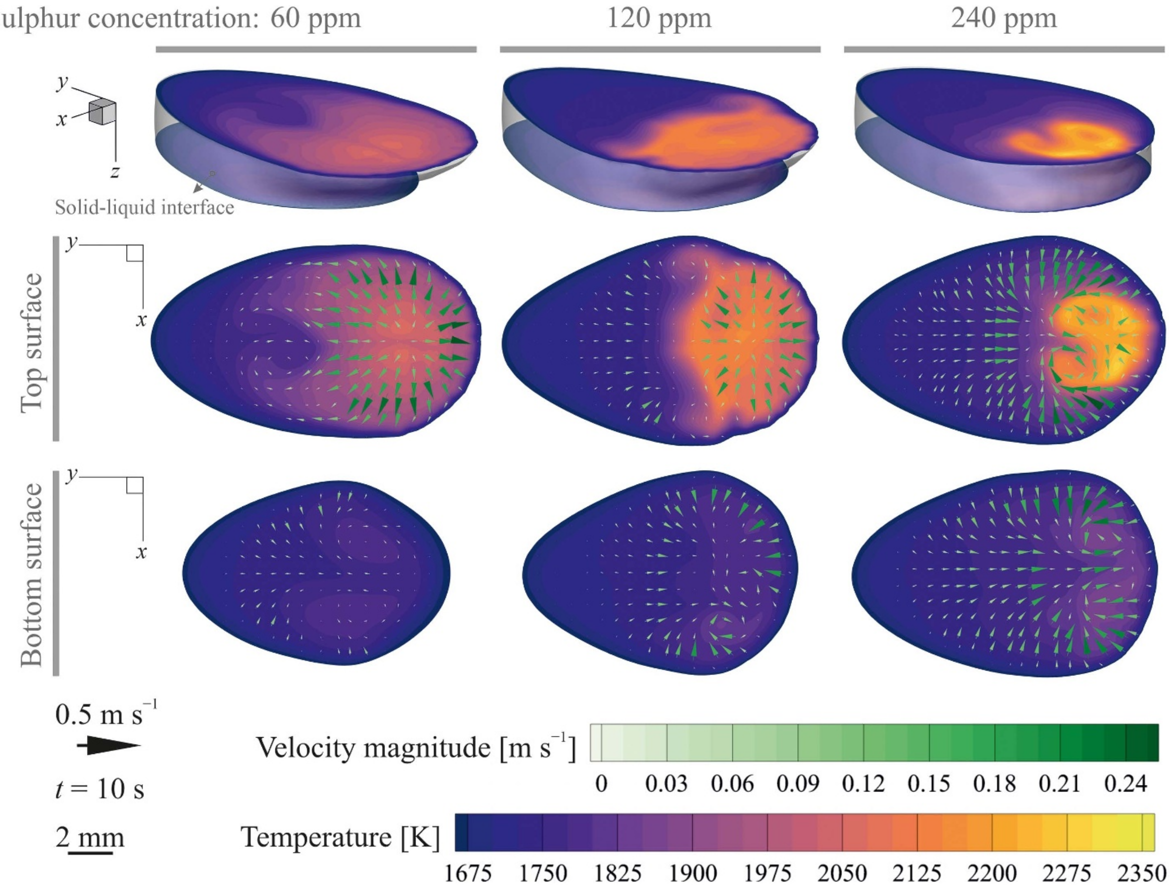

Figure 11. The influence of sulphur concentration in the material on the melt-pool shape during gas tungsten arc welding. Contours show the temperature profile at $t = 10$ s and are overlaid with velocity vectors. The 0.5 $\mathrm{m\,s^{-1}}$ reference vector is provided for scaling the velocity field. ($I = 85$ A, travel speed: 2.5 $\mathrm{mm\,s^{-1}}$ and welding position: C1.)

compared to that of the case C1 and C5, changing the oscillation frequency as reflected in figure 5. The results suggest that when the relative material thickness (H/H_m) beneath the welding torch reduces to values less than about 0.65, an unsteady multicellular flow pattern evolves in the pool [18, 77], leading to irregular surface deformations that are reflected in the time-frequency spectra shown in figure 5(b) and d) for $t > 6$ s.

Figure 11 shows the melt-pool shape and thermal and flow fields over the melt-pool surfaces at $t = 10$ s for GTA welding in welding position C1 with a travel speed of 2.5 $\mathrm{mm\,s^{-1}}$ and different sulphur concentrations in the material. The results of the present numerical simulations suggest that both the amplitude and frequency of oscillations decrease with reducing the sulphur concentration in the material. Reducing sulphur concentration in the material results in an increase in the average surface tension of the molten material, affects the variation of surface tension with temperature ($\partial\gamma/\partial T$) and reduces the critical temperature at which the sign of the temperature gradient of surface tension ($\partial\gamma/\partial T$) changes, according to (21) (see figure 2). The flow pattern over the melt-pool top surface becomes mostly outward when the sulphur concentration in the material is reduced. The increasingly outward fluid flow weakens disturbances caused by the interaction of inward and outward fluid flows over the melt-pool surface. Additionally, the outward fluid flow transfers the heat absorbed by the material towards the melt-pool boundary, reducing the maximum temperature and the magnitude of temperature gradients over the melt-pool surface. Moreover, the outward flow results in a relatively larger melt-pool surface area on the top surface compared to that on the bottom surface and fluid velocities decrease on the bottom surface. These changes in the flow field alter the melt-pool shape, as shown in figure 11, and in turn affects the melt-pool oscillatory behaviour. A notable change in the time-frequency spectra of the cases with sulphur concentrations of 120 ppm and 60 ppm (figure 6) compared to that with a sulphur concentration of 240 ppm (figure 4(a)) is that the frequency of oscillations decreases gradually over time and does not change suddenly as observed in figure 4(a) at $t \approx 4$ s.

The influence of travel speed on melt-pool shape and heat and fluid flow in the melt pool during GTA welding in position C1 is shown in figure 12 for the cases with a sulphur concentration of 240 ppm. Increasing the travel speed, while keeping other process parameters the same, results in a decrease in the melt-pool size, which is due to the reduction of nominal heat input to the material. Additionally, the melt-pool shape changes from a virtually circular shape to a teardrop shape with increasing travel speed. The flow pattern obtained from the numerical simulations also reveals that vortex structures do

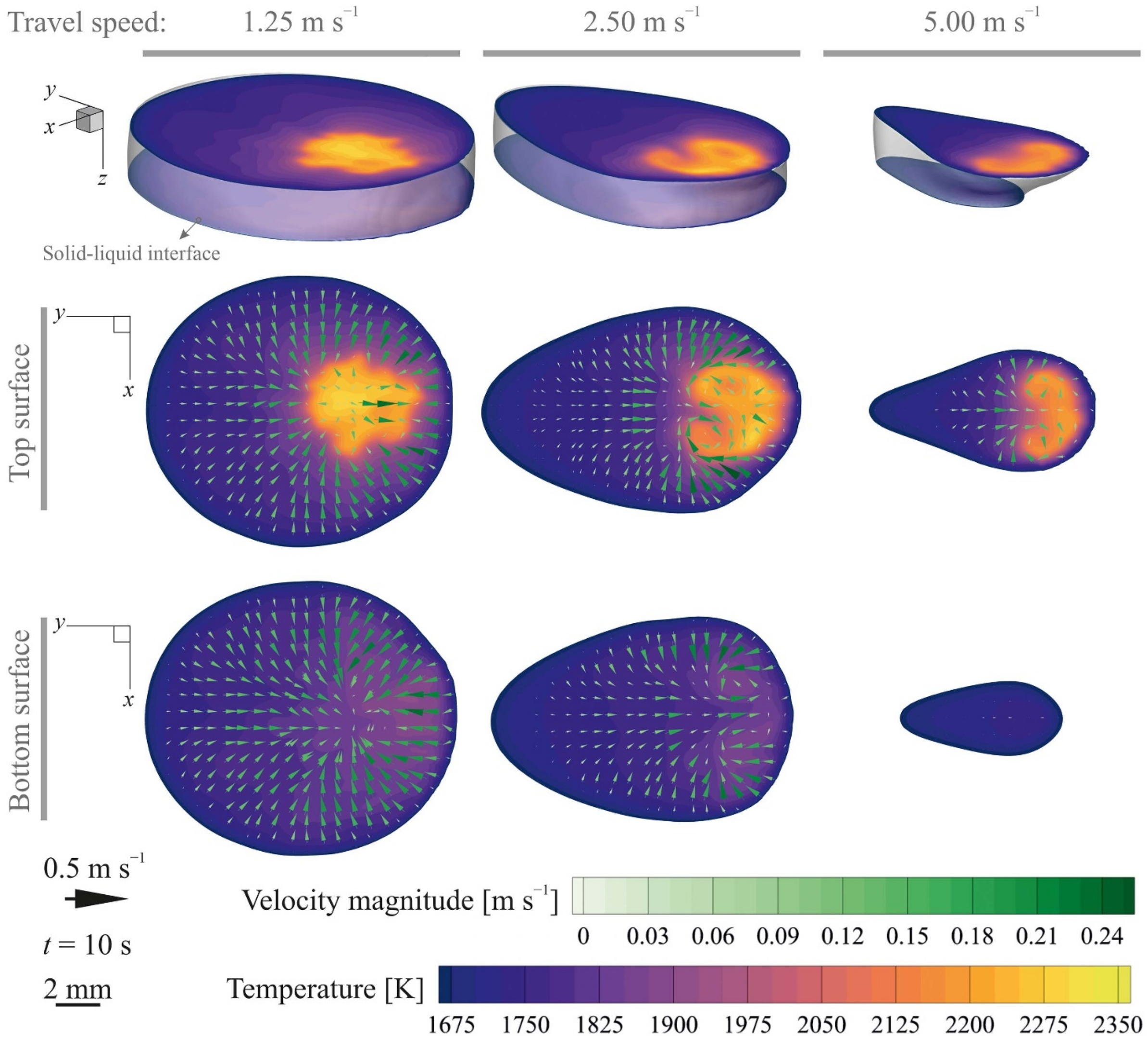

Figure 12. The influence of travel speed on the melt-pool shape during gas tungsten arc welding. Contours show the temperature profile at $t = 10$ s and are overlaid with velocity vectors. The 0.5 $\mathrm{m\,s^{-1}}$ reference vector is provided for scaling the velocity field. ($I = 85$ A, sulphur concentration: 240 ppm and welding position: C1.)

not form over the melt-pool surface for the case with a travel speed of 1.25 $\mathrm{mm\,s^{-1}}$, in contrast to other cases with higher travel speeds. Moreover, the offset between the top and bottom melt-pool surfaces increases with increasing the travel speed. The offset measured at the leading edge of the pool with respect to the z-axis increases from about 5° at a travel speed of 1.25 $\mathrm{mm\,s^{-1}}$ to values of about 50° at a travel speed of 5 $\mathrm{mm\,s^{-1}}$.

6. Conclusions

High-fidelity three-dimensional numerical simulations were performed to study the oscillatory behaviour of fully-penetrated melt pools during positional gas tungsten arc welding. The influence of welding positions, the sulphur concentration in the material and travel speed on complex unsteady convection in the melt pool and oscillations of the melt-pool surface were investigated. The frequencies predicted using the present computational model are compared with analytical and experimental data, and reasonably good agreement (within 5% deviation bands) is achieved. Using the present numerical approach, evolutions of the melt-pool surface oscillations during GTA welding are described by revealing the unsteady complex flow pattern in the melt pools and subsequent changes in the melt-pool shape, which are generally difficult to visualise experimentally. Moreover, evolution of the frequency of melt-pool oscillations during arc welding are not predictable using the analytical models that are available in the open literature.

Melt-pool oscillatory behaviour depends on surface tension of the molten material and shape and size of the melt-pool. Changes in material properties and welding process parameters affect convection in the melt pool, hydrodynamic instabilities that arise and resultant variations in the melt-pool shape. Depending on the processing condition, these instabilities can also grow in time, affecting melt-pool stability and may even lead to melt-pool collapse and process failure. Welding position affects the melt-pool surface morphology, altering the spatial distribution of arc forces and power-density applied to the molten material and thus changes flow pattern in the melt-pool. The change in the flow pattern affects the evolution of the melt-pool shape and its oscillatory behaviour. The frequency of oscillations seems to vary within the same range (22 Hz $< f <$ 73 Hz) for different welding positions studied in the present work, however the evolution of oscillation frequencies, which depends on the melt-pool shape, is affected by welding position. Under similar welding conditions, sulphur concentration in the material significantly affects the thermal and flow fields in the melt pool and consequently the shape of the pool, changing the oscillatory behaviour of the melt-pool. Increasing the travel speed decreases the melt-pool size, increases the offset between top and bottom melt-pool surfaces and also affects the flow structures (vortex formation) on the melt-pool surface. These observations offer an insight into the complex melt-pool oscillatory behaviour during positional gas tungsten arc welding and suggest that the processing window for advanced fusion-based manufacturing processes can be determined by utilising numerical simulations that can potentially reduce the costs associated with process development and optimisation.

Data availability statement

The raw/processed data required to reproduce these findings cannot be shared at this time due to their large size, but representative samples of the research data are presented in the paper. Other datasets generated during this study are available from the corresponding author on reasonable request. All data that support the findings of this study are included within the article (and any supplementary files).

Acknowledgment

This research was carried out under Project Number F31.7.13504 in the framework of the Partnership Program of the Materials innovation institute M2i (www.m2i.nl) and the Foundation for Fundamental Research on Matter (FOM) (www.fom.nl), which is part of the Netherlands Organisation for Scientific Research (www.nwo.nl). The authors would like to thank the industrial partner in this project 'Allseas Engineering B.V.' for the financial support.

Author Contributions

Conceptualisation, A E, C R K and I M R; methodology, A E; software, A E; validation, A E; formal analysis, A E; investigation, A E; resources, A E, C R K, M J M H, and I M R; data curation, A E; writing—original draft preparation, A E; writing—review and editing, A E, C R K, M J M H, and I M R; visualisation, A E; supervision, C R K and I M R; project administration, A E and I M R; and funding acquisition, I M R.

Conflict of interest

The authors declare no conflict of interest.

ORCID iDs

Amin Ebrahimi https://orcid.org/0000-0002-4912-2549
Chris R Kleijn https://orcid.org/0000-0001-6821-0969
Marcel J M Hermans https://orcid.org/0000-0002-6204-5285
Ian M Richardson https://orcid.org/0000-0002-3651-3233

References

[1] Aucott L *et al* 2018 Revealing internal flow behaviour in arc welding and additive manufacturing of metals *Nat. Commun.* **9** 5414

[2] DebRoy T and David S A 1995 Physical processes in fusion welding *Rev. Mod. Phys.* **67** 85–112

[3] DebRoy T *et al* 2018 Additive manufacturing of metallic components–process, structure and properties *Prog. Mater. Sci.* **92** 112–224

[4] Mills K C and Keene B J 1990 Factors affecting variable weld penetration *Int. Mater. Rev.* **35** 185–216

[5] Juang S C and Tarng Y S 2002 Process parameter selection for optimizing the weld pool geometry in the tungsten inert gas welding of stainless steel *J. Mater. Process. Technol.* **122** 33–37

[6] Cunningham R, Zhao C, Parab N, Kantzos C, Pauza J, Fezzaa K, Sun T and Rollett A D 2019 Keyhole threshold and morphology in laser melting revealed by ultrahigh-speed x-ray imaging *Science* **363** 849–52

[7] Lancaster J F (ed) 1986 *The Physics of Welding* (*International Series on Materials Science of Technology*) 2nd edn (Oxford: Pergamon)

[8] Li C, Shi Y, Du L, Yufen G and Zhu M 2017 Real-time measurement of weld pool oscillation frequency in GTAW-P process *J. Manuf. Process.* **29** 419–26

[9] Shi Y, Zhang G, Ma X J, Gu Y F, Huang J K and Fan D 2015 Laser-vision-based measurement and analysis of weld pool oscillation frequency in GTAW-P *Weld J.* **94** 176s–87s

[10] Xiao Y H and den Ouden G 1990 A study of GTA weld pool oscillation *Weld J.* **69** 289s–93s

[11] Yoo C D and Richardson R W 1993 An experimental study on sensitivity and signal characteristics of welds pool oscillation *Trans. Japan Weld. Soc.* **24** 54–62

[12] Tam A S and Hardt D E 1989 Weld pool impedance for pool geometry measurement: stationary and nonstationary pools *J. Dyn. Syst. Meas. Control* **111** 545–53

[13] Xiao Y H 1992 Weld pool oscillation during gas tungsten arc welding PhD Dissertation Delft University of Technology (available at: https://resolver.tudelft.nl/uuid:f91da1e6-1a17-4223-9d73-419f1ac9c312)

[14] Xiao Y H and den Ouden G 1993 Weld pool oscillation during GTA welding of mild steel *Weld J.* **72** 428s–34s

[15] Andersen K, Cook G E, Barnett R J and Strauss A M 1997 Synchronous weld pool oscillation for monitoring and control *IEEE Trans. Ind. Appl.* **33** 464–71

[16] Maruo H and Hirata Y 1993 Natural frequency and oscillation modes of weld pools. 1st report: weld pool oscillation in full penetration welding of thin plate *Weld. Int.* **7** 614–19
[17] Wu F, Falch K V, Guo D, English P, Drakopoulos M and Mirihanage W 2020 Time evolved force domination in arc weld pools *Mater. Des.* **190** 108534
[18] Ebrahimi A, Kleijn C R and Richardson I M 2021 A simulation-based approach to characterise melt-pool oscillations during gas tungsten arc welding *Int. J. Heat Mass Transfer* **164** 120535
[19] Cook P S and Murphy A B 2020 Simulation of melt pool behaviour during additive manufacturing: underlying physics and progress *Addit. Manuf.* **31** 100909
[20] Kou S and Sun D K 1985 Fluid flow and weld penetration in stationary arc welds *Metall. Trans.* A **16** 203–13
[21] Zacharia T, Eraslan A H, Aidun D K and David S A 1989 Three-dimensional transient model for arc welding process *Metall. Trans.* B **20** 645–59
[22] Wu C S and Dorn L 1994 Computer simulation of fluid dynamics and heat transfer in full-penetrated TIG weld pools with surface depression *Comput. Mater. Sci.* **2** 341–9
[23] Wu C S, Chen J and Zhang Y M 2007 Numerical analysis of both front- and back-side deformation of fully-penetrated GTAW weld pool surfaces *Comput. Mater. Sci.* **39** 635–42
[24] Mishra S, Lienert T J, Johnson M Q and DebRoy T 2008 An experimental and theoretical study of gas tungsten arc welding of stainless steel plates with different sulfur concentrations *Acta Mater.* **56** 2133–46
[25] Traidia A and Roger F 2011 Numerical and experimental study of arc and weld pool behaviour for pulsed current GTA welding *Int. J. Heat Mass Transfer* **54** 2163–79
[26] Mougenot J, Gonzalez J-J, Freton P and Masquère M 2013 Plasma–weld pool interaction in tungsten inert-gas configuration *J. Phys. D: Appl. Phys.* **46** 135206
[27] Hao H, Gao J and Huang H 2020 Numerical simulation for dynamic behavior of molten pool in tungsten inert gas welding with reserved gap *J. Manuf. Process.* **58** 11–18
[28] Thompson M E and Szekely J 1989 The transient behavior of weldpools with a deformed free surface *Int. J. Heat Mass Transfer* **32** 1007–19
[29] Tsai M C and Kou S 1989 Marangoni convection in weld pools with a free surface *Int. J. Numer. Methods Fluids* **9** 1503–16
[30] Kim S D and Na S J 1992 Effect of weld pool deformation on weld penetration in stationary gas tungsten arc-welding *Weld J.* **71** 179s–93s
[31] Zhang Y M, Cao Z N and Kovacevic R 1996 Numerical analysis of fully penetrated weld pools in gas tungsten arc welding *Proc. Inst. Mech. Eng.* C **210** 187–95
[32] Cao Z N, Zhang Y M and Kovacevic R 1998 Numerical dynamic analysis of moving GTA weld pool *J. Manuf. Sci. Eng.* **120** 173–8
[33] Liu J W, Rao Z H, Liao S M and Tsai H L 2015 Numerical investigation of weld pool behaviors and ripple formation for a moving GTA welding under pulsed currents *Int. J. Heat Mass Transfer* **91** 990–1000
[34] Meng X, Qin G, Bai X and Zou Z 2016 Numerical analysis of undercut defect mechanism in high speed gas tungsten arc welding *J. Mater. Process. Technol.* **236** 225–34
[35] Feng C, Qin G, Meng X and Geng P 2020 Defect evolution of 409L stainless steel in high-speed TIG welding *Mater. Manuf. Process.* **35** 179–86
[36] Du J, Zhao G and Wei Z 2019 Effects of welding speed and pulse frequency on surface depression in variable polarity gas tungsten arc welding of aluminum alloy *Metals* **9** 114
[37] Pan J, Hu S, Yang L and Wang D 2016 Investigation of molten pool behavior and weld bead formation in VP-GTAW by numerical modelling *Mater. Des.* **111** 600–7
[38] Chen Y, David S A, Zacharia T and Cremers C J 1998 Marangoni convection with two free surfaces *Numer. Heat Transfer* A **33** 599–620
[39] Ko S H, Yoo C D, Farson D F and Choi S K 2000 Mathematical modeling of the dynamic behavior of gas tungsten arc weld pools *Metall. Mater. Trans.* B **31** 1465–73
[40] Ko S H, Choi S K and Yoo C D 2001 Effects of surface depression on pool convection and geometry in stationary GTAW *Weld J.* **80** 39s–45s
[41] Sahoo P, Debroy T and McNallan M J 1988 Surface tension of binary metal—surface active solute systems under conditions relevant to welding metallurgy *Metall. Trans.* B **19** 483–91
[42] Joshi Y, Dutta P, Schupp P E and Espinosa D 1997 Nonaxisymmetric convection in stationary gas tungsten arc weld pools *J. Heat Transfer* **119** 164–72
[43] Zhao C X, van Steijn V, Richardson I M, Kleijn C R, Kenjeres S and Saldi Z 2009 Unsteady interfacial phenomena during inward weld pool flow with an active surface oxide *Sci. Technol. Weld. Join.* **14** 132–40
[44] Kidess A, Kenjereš S and Kleijn C R 2016 The influence of surfactants on thermocapillary flow instabilities in low Prandtl melting pools *Phys. Fluids* **28** 062106
[45] Kang N, Mahank T A, Kulkarni A K and Singh J 2003 Effects of gravitational orientation on surface deformation and weld pool geometry during gas tungsten arc welding *Mater. Manuf. Process.* **18** 169–80
[46] Nguyen M C, Medale M, Asserin O, Gounand S and Gilles P 2017 Sensitivity to welding positions and parameters in GTA welding with a 3D multiphysics numerical model *Numer. Heat Transfer* A **71** 233–49
[47] Tsai N S and Eagar T W 1985 Distribution of the heat and current fluxes in gas tungsten arcs *Metall. Trans.* B **16** 841–6
[48] Lin M L and Eagar T W 1986 Pressures produced by gas tungsten arcs *Metall. Trans.* B **17** 601–7
[49] Mills K C 2002 Fe-316 Stainless Steel *Recommended Values of Thermophysical Properties for Selected Commercial Alloys* (Amsterdam: Elsevier) pp 135–42
[50] Voller V R and Swaminathan C R 1991 General source-based method for solidification phase change *Numer. Heat Transfer* B **19** 175–89
[51] Hirt C W and Nichols B D 1981 Volume of fluid (VOF) method for the dynamics of free boundaries *J. Comput. Phys.* **39** 201–25
[52] Voller V R and Prakash C 1987 A fixed grid numerical modelling methodology for convection-diffusion mushy region phase-change problems *Int. J. Heat Mass Transfer* **30** 1709–19
[53] Ebrahimi A, Kleijn C R and Richardson I M 2019 Sensitivity of numerical predictions to the permeability coefficient in simulations of melting and solidification using the enthalpy-porosity method *Energies* **12** 4360
[54] Brackbill J U, Kothe D B and Zemach C 1992 A continuum method for modeling surface tension *J. Comput. Phys.* **100** 335–54
[55] Bai X, Colegrove P, Ding J, Zhou X, Diao C, Bridgeman P, roman Hönnige J, Zhang H and Williams S 2018 Numerical analysis of heat transfer and fluid flow in multilayer deposition of PAW-based wire and arc additive manufacturing *Int. J. Heat Mass Transfer* **124** 504–16
[56] Lee S Y and Na S J 1996 A numerical analysis of a stationary gas tungsten welding arc considering various electrode angles *Weld J.* **75** 269s–79s
[57] Lee S Y and Na S J 1995 Analysis of TIG welding arc using boundary-fitted coordinates *Proc. Inst. Mech. Eng.* B **209** 153–64
[58] Unnikrishnakurup S, Rouquette S, Soulié F and Fras G 2017 Estimation of heat flux parameters during static gas

tungsten arc welding spot under argon shielding *Int. J. Therm. Sci.* **114** 205–12

[59] Meng X, Qin G and Zou Z 2016 Investigation of humping defect in high speed gas tungsten arc welding by numerical modelling *Mater. Des.* **94** 69–78

[60] Tsao K C and Wu C S 1988 Fluid flow and heat transfer in GMA weld pools *Weld J.* **67** 70s–75s

[61] Tritton D J 1977 *Physical Fluid Dynamics* The Modern University in Physics Series (New York: Van Nostrand Reinhold Co.)

[62] Murphy A B and Lowke J J 2018 Heat transfer in arc welding *Handbook of Thermal Science and Engineering Kulacki F A* (Berlin: Springer) pp 2657–727

[63] Richardson I M 1991 Properties of the constricted gas tungsten (plasma) welding arc at elevated pressures PhD Thesis Industrial and Manufacturing Science, Cranfield Institute of Technology

[64] Goodarzi M, Choo R and Toguri J M 1997 The effect of the cathode tip angle on the GTAW arc and weld pool: I. Mathematical model of the arc *J. Phys. D: Appl. Phys.* **30** 2744–56

[65] Johnson K L, Rodgers T M, Underwood O D, Madison J D, Ford K R, Whetten S R, Dagel D J and Bishop J E 2017 Simulation and experimental comparison of the thermo-mechanical history and 3D microstructure evolution of 304L stainless steel tubes manufactured using LENS *Comput. Mech.* **61** 559–74

[66] Sridharan K, Allen T, Anderson M, Cao G and Kulcinski G 2011 Emissivity of candidate materials for VHTR applications: role of oxidation and surface modification treatments *Technical Report* (University of Wisconsin) (available at: www.osti.gov/biblio/1022709)

[67] ANSYS® Fluent 2018 *Release 19.2*

[68] Issa R I 1986 Solution of the implicitly discretised fluid flow equations by operator-splitting *J. Comput. Phys.* **62** 40–65

[69] Patankar S V 1980 *Numerical Heat Transfer and Fluid Flow* 1st edn (London: Taylor and Francis)

[70] Ubbink O 1997 Numerical prediction of two fluid systems with sharp interfaces Doctoral Thesis Imperial College London (University of London), London, United Kingdom (available at: https://hdl.handle.net/10044/1/8604)

[71] Ebrahimi A, Kleijn C R and Richardson I M 2019 The influence of surface deformation on thermocapillary flow instabilities in low Prandtl melting pools with surfactants *Proc. 5th World Congress on Mechanical, Chemical and Material Engineering* (Avestia Publishing)

[72] Ebrahimi A, Kleijn C R and Richardson I M 2020 Numerical study of molten metal melt pool behaviour during conduction-mode laser spot melting *J. Phys. D: Appl. Phys.* **54** 105304

[73] Yudodibroto Y B 2010 Liquid metal oscillations and arc behaviour during welding PhD Dissertation Delft University of Technology (available at: https://resolver.tudelft.nl/uuid:dcae1f78-9186-4161-ad88-711f27781335)

[74] Rioul O and Vetterli M 1991 Wavelets and signal processing *IEEE Signal Process. Mag.* **8** 14–38

[75] Mallat S 2009 *A Wavelet Tour of Signal Processing* (Amsterdam: Elsevier)

[76] Li C, Shi Y, Gu Y and Yuan P 2018 Monitoring weld pool oscillation using reflected laser pattern in gas tungsten arc welding *J. Mater. Process. Technol.* **255** 876–85

[77] Schatz M F and Neitzel G P 2001 Experiments on thermocapillary instabilities *Annu. Rev. Fluid Mech.* **33** 93–127